J. Fluid Mech. (2002), *vol.* 450, *pp.* 297–316.
DOI: 10.1017/S0022112001006413 Printed in the United Kingdom

Convection in a spherical capacitor

By KAMEL AMARA† AND JOHN HEGSETH
Department of Physics, University of New Orleans, New Orleans, LA 70148, USA

(Received 23 May 1999 and in revised form 15 June 2001)

Real-time holographic interferometry and shadowgraph visualization are used to study convection in the fluid between two concentric spheres when two distinct buoyancy forces are applied to the fluid. The heated inner sphere has a constant temperature that is greater than the constant temperature of the outer sphere by ΔT. In addition to the usual gravitational buoyancy from temperature induced density differences, another radial buoyancy is imposed by applying an a.c. voltage difference, ΔV between the inner and outer spheres. The resulting electric field gradient in this spherical capacitor produces a central polarization force. The temperature dependence of the dielectric constant results in the second buoyancy force that is especially large near the inner sphere. The normal buoyancy is always present and, within the parameter range explored in our experiment, always results in a large-scale cell that is axisymmetric about the vertical. We have found that this flow becomes unstable to toroidal or spiral rolls that form near the inner sphere and travel vertically upward when ΔT and ΔV are sufficiently high. These rolls start near the centre sphere's equator and travel upward toward its top. The onset of this instability depends on both the temperature difference at onset ΔT_c and the voltage difference at onset ΔV_c and these two quantities appear to be related, within the parameter range accessible to our experimental system, by a power law $\Delta V_c \propto \Delta T_c^{1/3}$. Measurements of the heat transfer show that these travelling rolls increase the heat transfer at onset. Far above onset, the heat transfer may actually decrease with increasing ΔT. The travelling roll's frequency increases with increasing ΔT near onset and with increasing ΔV far above onset. These results have been interpreted in terms of a flow structure that includes a thermal boundary-layer-like behaviour. This layer has a radial width that increases from the bottom pole to an unstable 'latitude' near the equator where the rolls appear.

1. Introduction

Thermal convection in spherical geometry includes many important situations in physics, chemistry and engineering (Chandrashakar 1961; Cloot & Lebon 1990; Hegseth, Rashidnia & Chai 1996). Spherical geometry is also important in geophysical flows, which provide insights into climatology, geology, meteorology and planetary science, as well as inspiring such concepts such as deterministic chaos and two-dimensional turbulence (Lorenz 1976). In planetary atmospheres, oceans, mantles and cores, the rapid rotation, the density stratification, and the spherical geometry are considered fundamental features in large-scale geophysical fluid dynamics (Pedlosky 1979; Cushman-Roisin 1994). The latitude dependent Coriolis force and the strongly

† Current address: Applied optics Center of Delaware, Delaware State University, 1200 N Dupont Highway, Dover, DE 19901-2277, USA.

nonlinear equations of motion in geophysical fluid flows have led to a dependency on asymptotic mathematical methods and computational methods for theoretical understanding. The small expansion parameters used in asymptotic methods allow only a small window of the parameters of the system to be studied. This method may, for example, limit the validity to a small region in latitude, called a beta plane, and cannot analyse global circulation. Numerical models are remarkable in that they can do much to simulate geophysical flows (Fletcher 1991). They try to include many important effects, such as geographical influences on the boundary layer, condensation and precipitation of water, and radiation heat transfer. These methods are limited, however, by the large difference in the spatial and temporal scales of the many structures that are strongly coupled through the nonlinear interactions, especially on the global scale. As in many turbulence simulations, representing the small-scale features of the flow requires using some *ad hoc* assumptions because of computational limitations (Minier 1998). This procedure may miss many nonlinear interactions between the structures at different scales.

Many of the data regarding geophysical flows have come from direct planetary observations where there are only a few cases available, corresponding to a small subset of the possible values of the control parameters for this class of flows. Although no experimental system is perfect, nonlinear interactions over a large-scale range are retained and control parameters may be continuously tuned in a wide range. At the very least, a well-controlled experiment can provide important information to help validate numerical models. As emphasized in many previous works, understanding geophysical flows when driven by thermal forcing from buoyancy is of a great importance (Carrigan & Busse 1983). In a well-controlled experimental system, simplifications to the 'real' situation can be made so that competing effects, that often occur simultaneously, can be eliminated and examined separately. In our experimental system discussed below, several such simplifications have been made. Specifically, our experimental system has a central-force applied to an incompressible fluid in spherical geometry. It is also roughly similar in geometry to a planetary liquid outer core. The central force is created using an a.c. electric field in a spherical capacitor filled with dielectric fluid between the spheres. Because of the temperature dependence of the dielectric constant and the temperature dependence of the fluid density, two buoyancy forces drive this flow when the inner sphere is heated to a higher temperature than the outer sphere.

Our system is limited in geophysical similarity because it is not rotated and it is also subjected to the usual gravitational buoyancy force from the Earth that breaks the spherical symmetry. Our system is, however, analogous to some astrophysical situations where a spherical body is subjected to both a central force and non-central forces such as a strong tidal interaction in a binary planet or a binary star system.

2. Background

An electric field influences a dielectric fluid in several ways. These influences include the modification of the thermodynamics of a fluid and the mechanical body force exerted on a fluid in a non-uniform field (Landau & Lifshitz 1960, 1982). Because the electric field produces both attractive and repulsive forces on positive or negative charges, it can produce many different bulk effects. These effects include the force on any charged fluid element and the polarization of the charge distribution of non-polar molecules to produce a dipole moment. This induced dipole moment is created because the average positions of the positive and negative bound charges in

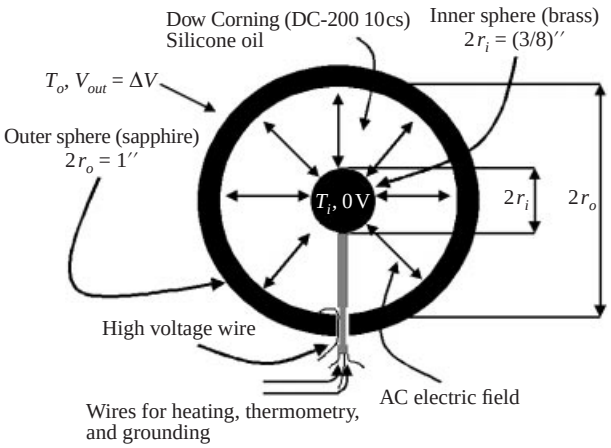

FIGURE 1. A cross-section of the experimental apparatus. The inner sphere, made of brass, is electrically earthed, has a thermocouple embedded in it to measure temperature, and is heated with a nichrome wire coil glued near its centre. A high voltage $V = \Delta V$ is applied to the outer sapphire sphere while the inner sphere is earthed. r_i is the outer radius of the inner sphere, r_o is the inner radius of the outer sphere, and the gap between the spheres, d, is $d = r_o - r_i$. The dimensionless gap or the aspect ration, Γ, is defined using r_i as a length scale, $\Gamma = d/r_i$.

a molecule become spatially separated as the field pulls the nucleus in one direction and the electrons in the opposite direction. If a molecule has a permanent dipole moment then the field produces a torque that tends to align the charge with the electric field. In other words, the positively charged portion of the molecule is forced in the direction of the field and vice versa for the negatively charged portion. In a non-uniform field, or an electric field gradient, such a polarized molecule feels a net force from the field toward the region of higher field intensity (i.e. the charge at the higher field intensity always feels a stronger force than the other charge). The result, in the continuum limit is a body force in the fluid (Landau & Lifshitz 1960, 1982). In an a.c. field, the dipole moment remains aligned with the field, preserving the attraction toward the higher field intensity.

In spherical geometry, such as concentric spheres with dielectric fluid between them (the spherical capacitor) shown in figure 1, the electric field gradient produces a central body force. When the central sphere is heated, the change in the dielectric constant with temperature (i.e. $\gamma = \gamma(T)$ where γ is the dielectric variability) produces a buoyancy in the presence of the polarization force field. This effect has been used previously to provide results of geophysical significance by also rotating the system including banana cells (rapid rotation and heating), soccer-pattern (heating and slow rotation), turbulence, Hadley cells (Hart 1976; Hart, Glatzmaier & Toomre 1986) (low rotation and buoyancy from terrestrial g). The buoyancy from the earth's gravity was avoided in these experiments by performing them in the weightlessness of an orbiting spacecraft. If the system is too large, it is difficult to obtain an appreciable effective gravity compared to g (g is the acceleration due to terrestrial gravity, 9.8 m s^{-1}) using an electric field below the breakdown voltage. We have found, however, that it is possible to obtain such a large effective gravity in a small system (Hegseth, Garcia & Amara 1999) creating the possibility of terrestrial experiments where normal buoyancy is comparable to the buoyancy from the polarization force. Unfortunately, such a small system makes it difficult to obtain a small aspect ratio, Γ, that would be similar to typical atmosphere or ocean where Γ is defined in figure 1. There are, however, other geophysi-

cal systems, such as a planetary core, that have a large aspect ratio. In the following, we present an experimental study of an instability caused by the radial buoyancy from an imposed electric field gradient and an imposed temperature gradient in spherical geometry without rotation, as a first step in studying large-scale geophysical flows.

3. Experimental conditions

If the dielectric properties of the fluid change from point to point then a uniform field may exert a force on the fluid. By contrast, a non-uniform field will exert a force on a uniform dielectric owing to the net force that such an electric field gradient exerts on each dipole, as discussed above. The net *pondermotive* force (per unit volume) is,

$$f = \rho_q E - \tfrac{1}{2}\varepsilon_0 \boldsymbol{E}^2 \nabla\kappa + \tfrac{1}{2}\varepsilon_0 \nabla\left(\boldsymbol{E}^2 \frac{\mathrm{d}\kappa}{\mathrm{d}\rho}\rho\right), \tag{1}$$

where ρ_q and ρ are the charge and mass density, respectively, E is the electric field, ε_0 and ε are the permitivity of free space and the fluid, respectively, and $\kappa = \varepsilon/\varepsilon_0$ is the dielectric constant $\rho_q \boldsymbol{E}$ is the force per unit volume on any free charges in the fluid (the electrophoretic force), $(\frac{1}{2}\varepsilon_0)E^2\nabla\kappa$ is sometimes called the dielectrophoretic force, and $(\frac{1}{2}\varepsilon_0)\nabla\{E^2(\mathrm{d}\kappa/\mathrm{d}\rho)\rho\}$ is sometimes called the electrostrictive force (Stratton 1941).

The electrophoretic force is typically large compared to the other forces in (1). All dielectric media have a small amount of ρ_q making an electrophoretic force. This effect can complicate or dominate the dielectrophoretic and electrostrictive effects. However, it is possible to define a relaxation time, τ, for free charge carriers subjected to an electric field, $\rho_q = \rho_{q0}\mathrm{e}^{-t/\tau}$ where $\tau = \kappa\varepsilon_0/\sigma$, and σ is the conductivity of the fluid. If this relaxation time, τ, is large compared to the period, T_f, of an a.c. field ($\tau \gg T_f$), then the charge carriers will not have time to respond to the applied field, essentially eliminating the $\rho_q E$ force, any current, and ohmic heating from such a current. The other two forces, depending on E^2, will not be similarly affected.

The inner sphere is positioned in the centre of the outer sphere, to within 0.2%, by using several stiff electrically conductive wires for grounding, heating current, and a thermocouple. In an ideal spherical capacitor with a potential difference, ΔV, applied between the inner sphere of radius r_i and the outer sphere of radius r_o, the electric field is in the radial direction with a magnitude of:

$$E = \frac{\Delta V r_i r_o}{dr^2} \tag{2}$$

with a gap between the spheres of $d = r_o - r_i$. This electric field is distorted from a radial field in the region of the wires. We have minimized this distortion by twisting the wires together when they pass through the fluid to the inner sphere. We have also run our experiment both with the wires going up and with the wires going down. We have not seen any qualitative or quantitative difference in the experimental results between these two orientations.

As discussed above, the dielectrophoretic force in an incompressible fluid generates a buoyancy force associated with the temperature change in the dielectric constant. This change, $\kappa = \kappa_a(1 - \gamma\Delta T)$, is analogous to the buoyancy from density changes $\rho = \rho_a(1 - \beta\Delta T)$ (κ_a is the ambient dielectric constant, γ is the dielectric variability $\gamma = \Delta\kappa/(\kappa_a\Delta T)$, ρ_a is the ambient density, and β is the thermal expansion coefficient). In fact, the buoyancy from dielectric variations reproduces the Bousinesq equations of motion with the forcing on the fluid in this approximation given by $\boldsymbol{F} = g_e\gamma\Delta T\boldsymbol{r}$ (Stratton 1941; Hegseth *et al.* 1999). This force has the same form as the usual

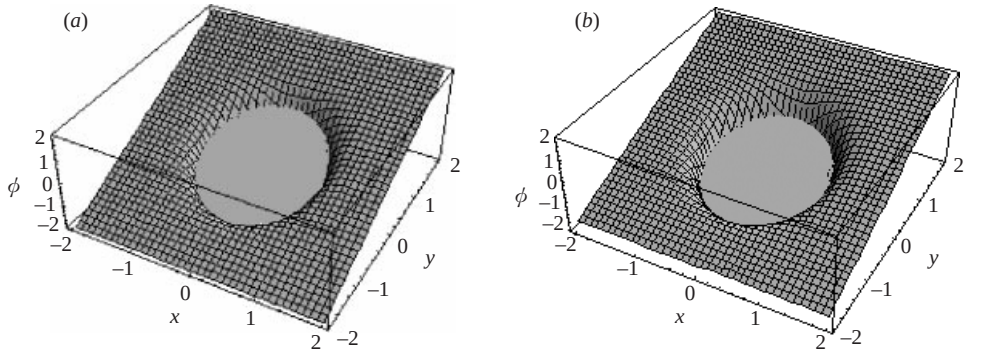

FIGURE 2. Plots of the potential energy from terrestrial gravity and the polarization force around the central sphere. The horizontal coordinate, x, and the vertical coordinate, y, are scaled by the inner sphere radius $r_i = 4.76\,\text{mm}$. The potential energy, ϕ, is scaled by mgr_i. Shown are the potentials for two different ΔV values, in (a) $\Delta V = 3000\,\text{V}$ and in (b) $\Delta V = 4000\,\text{V}$. The effect of terrestrial gravity occurs throughout the gap between the spheres. The polarization force is largest at the inner sphere. The maximum polarization force per unit mass, g_e, is as high as $g_e \approx 2g$ in (b), where g is the acceleration due to gravity.

buoyancy forcing, $\boldsymbol{F} = g\beta\Delta T\boldsymbol{z}$, from density variations in normal gravity, but has a different orientation. In this incompressible case the equivalent gravity, g_e is given by

$$g_e = \frac{2\kappa\varepsilon_0}{\rho}\left(\frac{\Delta V r_o r_i}{d}\right)^2 \frac{1}{r^5}. \tag{3}$$

This equation gives appreciable equivalent gravity values for small cells at the inner sphere where the force has a maximum value. Figure 2 shows several plots of the potential energy function of the above force superposed with the potential energy from normal gravity in our cell of $r_i = 4.76\,\text{mm}$, $r_o = 12.70\,\text{mm}$. It is clear from this figure that normal buoyancy dominates most of the volume of the sphere (i.e. there is a very small g_e value at the outer sphere). Very close to the inner sphere, however, we can see a very large slope, mostly from the potential energy of the polarization force. In fact, at the surface of the inner sphere g_e becomes as large as $g_e \approx 2g$ at 4 kV, where g is the acceleration due to gravity. Because β and γ are nearly equal in the Dow Corning 200 10 cs silicone oil (DC-200 10 cs, Prandtl number, $Pr = 10.5$) used in this experiment, we can see that our small system has a large possibility for instability near the inner sphere.

Our set-up, shown in figure 1, uses a spherical capacitor built from two concentric spheres. We use the inner sphere's radius r_i as the characteristic length of the spherical capacitor so that the aspect ratio is $\Gamma = d/r_i = 1.67$. The aspect ratio, or the dimensionless gap length, is a single parameter that characterizes the geometry of this system. This brass inner sphere ($r_i = 4.76\,\text{mm}$) is grounded and heated with a Nichrome wire coil glued near the centre of the inner sphere. A thermocouple, also near the centre of the inner sphere, gives a temperature reading, T_i, in the inner sphere. The characteristic time for heat transport in the inner sphere is $r_i^2/\kappa_B = 0.6\,\text{s}$, where r_i is the radius of the inner sphere and κ_B is the thermal diffusivity of brass. Because this time is much smaller than $d^2/\kappa_S = 624\,\text{s}$, where d is the gap between the spheres and κ_S is the thermal diffusivity of the DC-200 10 cs silicone, we see that T_i is the same throughout the inner sphere to a very good approximation. The outer sphere, of inner diameter $2r_e = 25.4\,\text{mm}$, is made of two 6.35 mm thick transparent sapphire hemispherical domes to allow optical diagnostics and good thermal conduction (i.e.

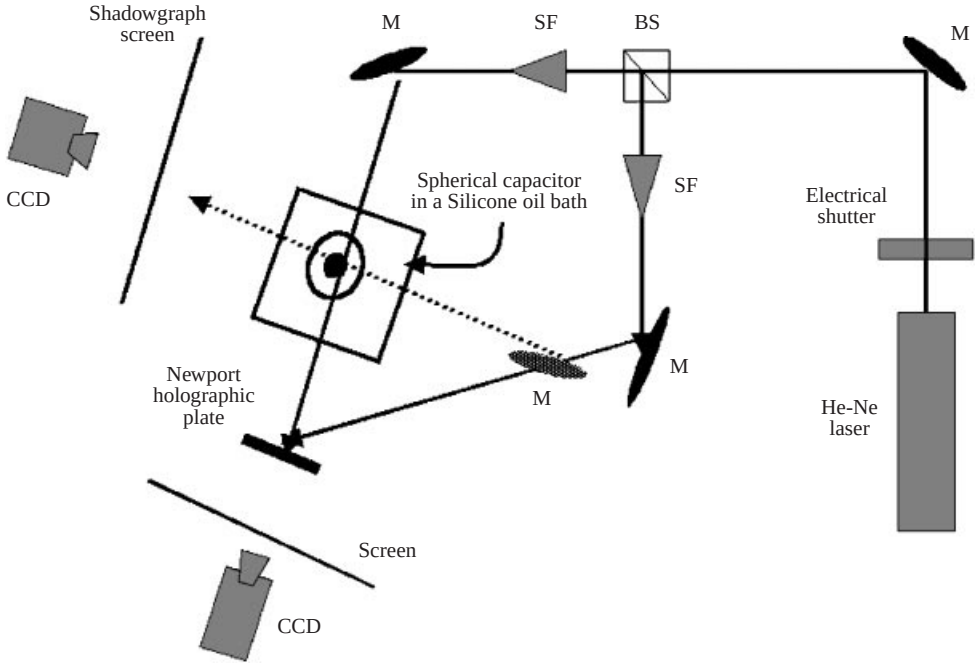

FIGURE 3. The optical set-up for holographic interferometry visualization and shadowgraph visualization. This configuration allows two perpendicular visualizations to be made simultaneously. M, mirror; BS, beam splitter; SF, spatial filter.

thermal conduction time of 2.8 s). A thermocouple is in contact with the outer sphere wall to monitor the temperature of the outer sphere. The whole capacitor is put inside a silicone oil bath of DC-200 10 cs, so that this fluid fills the capacitor gap ($d = 7.94$ mm). The bath temperature is controlled by a temperature controlled external water bath. The experiments are conducted by keeping the outer sphere temperature, T_o, constant and slightly elevated from room temperature (usually at $19\,^{\circ}\mathrm{C} \pm 0.1\,^{\circ}\mathrm{C}$). The temperature of the inner sphere, T_i, is computer controlled in the range of $19 \pm 0.1\,^{\circ}\mathrm{C}$ to $47 \pm 0.1\,^{\circ}\mathrm{C}$, so that the temperature difference $\Delta T = T_i - T_o$ can range between $0\,^{\circ}\mathrm{C}$ and $28\,^{\circ}\mathrm{C}$. The outer sphere is connected to a high voltage a.c. transformer driven by a variable voltage and variable frequency power supply. This high voltage, ΔV, applied across the capacitor could be set from 0 kV to 5 kV (± 10 V) at a frequency of 300 Hz. The field thus reverses polarity in a period much shorter than the charge relaxation time, $\tau = 221$ s for the fluid. This ensures an absence of d.c. electric currents and associated effects as discussed above. The high-voltage a.c. source created large signal fluctuations that decreased T_i (and ΔT) values for high ΔV values. This problem was solved by compensation in the computer control.

Real-time holographic interferometry was used to visualize the flow when the heating and/or the voltage were applied. This optical technique allows *in situ* observation of a continuously changing process, whereas the usual double exposure technique is only able to capture phenomena at an instant in time (Vest 1979). This technique gives a quantitative measure of the average change in index of refraction along the beam path. The beam path is perpendicular to the image that shows the fringes. This index change can be directly related to the average temperature field. Shadowgraph visualization was also used at higher ΔT when light refraction became large. At higher ΔT, our visualization typically consisted of a shadowgraph image near the inner

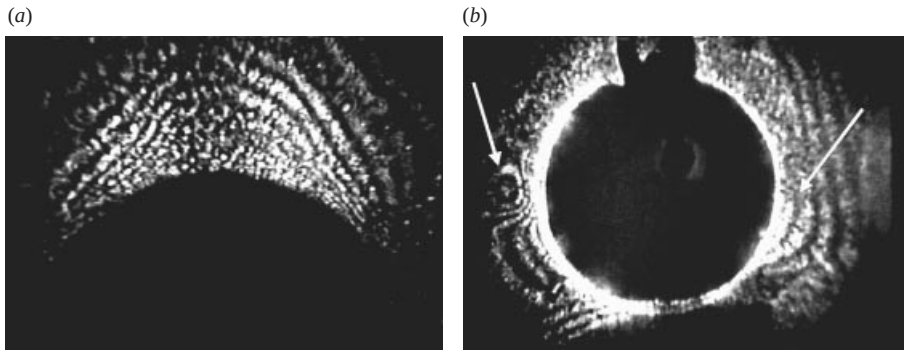

FIGURE 4. (*a*) Interference fringes that form above the inner sphere from hot fluid that flows upward under the influence of normal buoyancy at $R_g = 4.8 \times 10^4$ ($\Delta T = 4\,^{\circ}\mathrm{C}$). This thermal forcing exists without an imposed ΔV and creates a large axisymmetric Hadley cell. (*b*) Several transient cells, indicated by the arrows, that form when $\Delta V = 4\,\mathrm{kV}$ ($R_{Emax} = 105.6$) is suddenly imposed in the Hadley cell at $R_g = 3.0 \times 10^4 (\Delta T = 2.5\,^{\circ}\mathrm{C})$. Cells such as these appear with equal probability at any position along the outer surface of the inner sphere. These are transient rolls and will be replaced by steady-state travelling rolls if ΔV remains present.

sphere, where refraction effects were large, together with interference fringes farther away from the inner sphere. A schematic diagram of the optical system used in our experiment is shown in figure 3. A 20 mW He-Ne laser exposed a Newport HC-300 thermoplastic holographic plate. The reference hologram was exposed and automatically developed *in situ* while the capacitor was at uniform ambient temperature. The holographic plate was continuously illuminated by the original reference beam, while the object beam crossed the capacitor at different temperatures and voltages, producing an interference pattern. Another simultaneous shadowgraph visualization was also made in an orientation perpendicular to the interferometric orientation, as shown in figure 3.

4. Results

We have observed a large-scale cell in the system whenever ΔT is applied between the two spheres by tracing dust particles in the spherical capacitor and observing the interference pattern. Because this cell may exist without an imposed ΔV, we conclude that this is a convective cell driven by the normal buoyancy from density changes. We characterize this buoyancy driving in the usual way by using the Rayleigh number, R_g, the ratio of the buoyancy force from g to the viscous force. Because our system has a ΔT between two spheres, there is always a horizontal temperature gradient so that there is always a flow. In our case, the Rayleigh number is defined by the expression:

$$R_g = \frac{\beta g \Delta T r_i^3}{\nu D_{th}} \tag{4}$$

Where r_i, β, ν and D_{th} are the characteristic length, the thermal expansion coefficient, the kinematic viscosity, and the thermal diffusivity, respectively. Figure 4(*a*) is an interferogram that shows the density change of the hot fluid above the inner sphere that drives this cell at $R_g = 4.8 \times 10^4$. The fluid heated close to the inner sphere moves upward under normal buoyancy, where g points in the downward direction. A returning flow moves downward by the outer sphere, driven by pressure gradients

(reaction forces required by continuity) and the downward buoyancy from the cooling near the outer sphere. These hot and cold currents form an axisymmetric toroidal cell that fills the gap between the spheres. We call this cell a 'Hadley' cell, by analogy with the Hadley cell in atmospheric dynamics (Guyot 1998).

When the Hadley cell is established at a given ΔT, we have applied a large central polarization force by applying a large ΔV between the spheres (as explained above $g_e \approx 2g$ near the inner sphere at 4 kV). We characterize the driving by the dielectric buoyancy force using another Rayleigh number, R_{Emax}, where:

$$R_{Emax} = \frac{2\gamma\kappa\varepsilon_0}{\nu D_{th}\rho(1-\eta)}\left(\frac{r_o}{d}\right)^2 \Delta V^2 \Delta T.$$

Because $R_{Emax} \propto \Delta V^2 \Delta T$, it depends on both external parameters. More details about R_{Emax} are given below. Just after applying a large voltage for a given temperature difference ΔT, we have seen rolls form close to the inner sphere. Individual rolls in this pattern are transient, lasting for only several seconds (e.g. 2 s for $R_g = 13.2 \times 10^4$ [$\Delta T = 11\,^{\circ}$C], and $R_{Emax} = 1045$[$\Delta V = 6$ kV]) and then vanishing. A roll can appear at all places around the inner sphere, including the bottom pole, with no apparent preferred position, as shown in figure 4(*b*) which shows a typical example where several transient rolls have formed just after applying $\Delta V = 4$ kV at $R_g = 3.0 \times 10^4$ ($\Delta T = 2.5\,^{\circ}$C and $R_{Emax} = 105.6$). This pattern of transient rolls also disappears after several seconds and a steady-state convection pattern appears. This steady-state convection consists of travelling rolls that occur only in the upper hemisphere. These travelling rolls start near the equator and propagate upward to the top pole. Because the rolls only exist when both ΔV and ΔT are applied, and only exist close to the inner sphere where the polarization force is large, we conclude that the dielectric buoyancy causes this flow.

We have systematically studied the onset of the travelling rolls by slowly increasing the central polarization force. At a given ΔT, with a steady Hadley cell present, we slowly increased ΔV between the spheres. At a threshold value of ΔV, we observed perturbations that start near the equator and travel along the inner sphere at a slight distance away from it. The interference fringes near the inner sphere show a slight radial displacement so that the oscillatory perturbations appear as transverse waves travelling in the polar direction. The amplitudes of these apparently transverse waves also increase as they travel. At higher ΔV, we see localized roll structures, that first appear near the equator, propagate toward the top pole where they disappear simultaneously on both sides of the inner sphere. Figure 5(*a*) shows a global view of the shadowgraph and interference pattern formed by these rolls. Figure 5(*b*) shows several close-up images of the interference pattern of the travelling rolls. Simultaneous shadowgraph observations, perpendicular to the holographic optic axis, have shown the same flow pattern (i.e. rolls appear, propagate upward, and disappear simultaneously in both orientations). We conclude that these rolls extend around the sphere forming toroidal or spiral roll patterns that travel upward. The travelling rolls always appear as ΔV is increased at all ΔT values possible in this experiment. We have also observed, prior to the onset of the propagating rolls, that increasing ΔV slightly decreases the interference fringe spacing. We have measured the ΔV values for the onset of convection for various ΔT (at given T_o) and the results are shown in figure 6. The ΔV values plotted are the ΔV when the first slow oscillations appear close to the inner sphere. The onset values of ΔV, shown in figure 6, were found by fixing the temperature difference ΔT and increasing ΔV until the oscillations could be seen in the interference pattern. As can be seen in the figure, at higher ΔT values

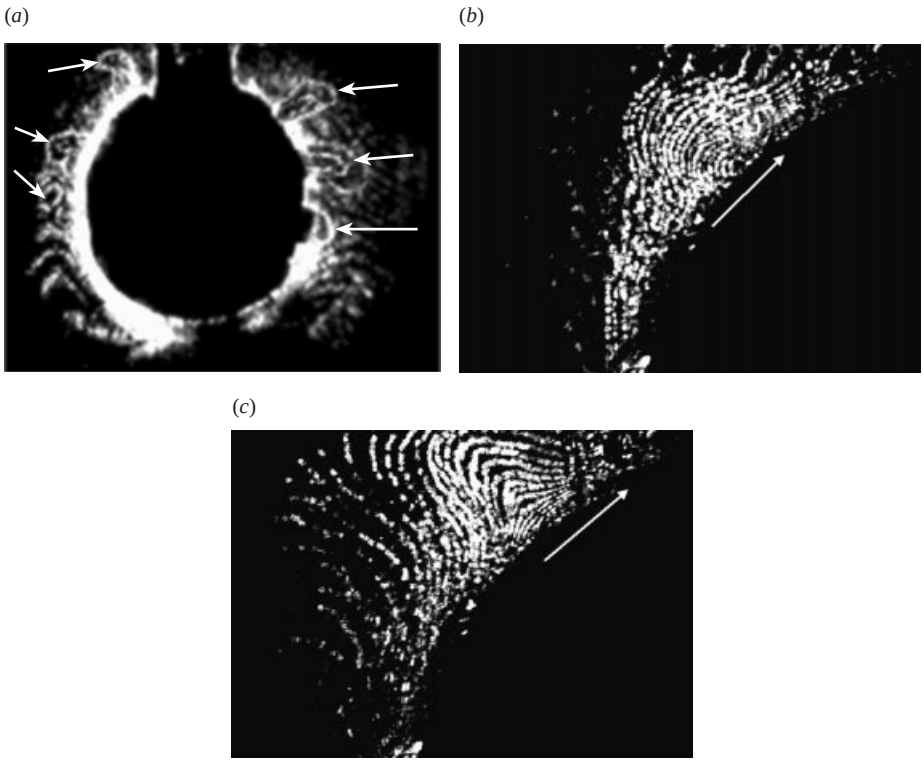

FIGURE 5. A global view of the travelling rolls, indicated by the arrows, at $R_g = 3.6\times10^4(\Delta T = 3.0\,^\circ\mathrm{C})$ and $R_{Emax} = 198.0(\Delta V = 5000\,\mathrm{V})$, where R_g and R_{Emax} are defined in the text. These rolls form at all values of $R_g \propto \Delta T$ when $R_E \propto \Delta V^2\Delta T$ is sufficiently increased. They also form near the equator and travel upward along the circumference of the inner sphere. (*b*) and (*c*) illustrate the propagation of these rolls by showing two close-up interferograms of a travelling roll (taken $\approx 1\,\mathrm{s}$ apart) as it travels toward the top pole, as indicated by the arrows, at $R_g = 1.3 \times 10^4(\Delta T = 1.1\,^\circ\mathrm{C})$ and $R_{Emax} = 72.6(\Delta V = 5000\,\mathrm{V})$.

the ΔV_c for onset decreased. Because the rolls disappear when ΔV is decreased below ΔV_c, with apparently no hysteresis, we conclude that we have observed a supercritical Hopf bifurcation to travelling rolls.

As the rolls propagate upward toward the top pole they produce a periodic signal in the interferogram. We have measured this oscillation frequency using a photodiode placed at a given point in the interferogram. The oscillation signal was digitized and then Fourier transformed producing a power spectrum. The power spectrum shows a frequency peak corresponding to the oscillation frequency of the propagating rolls. We found several regimes where this frequency showed interesting behaviour when external parameters were changed. The frequency of the propagating rolls was measured when ΔT was varied, at a fixed value of $\Delta V = 4\,\mathrm{kV}$ close to the onset of the propagating rolls, as shown in figure 7(*a*). The frequency of the travelling rolls was also measured far above the onset of the travelling rolls when ΔV was varied, at a fixed value of $\Delta T = 22\,^\circ\mathrm{C}$, as shown in figure 7(*b*). These fixed values of ΔV in figure 7(*a*) and ΔT in figure 7(*b*) were chosen to allow a wide range of parameter space to be observed in the travelling roll regime. We can see in both of these examples that the frequency monotonically increases. In the first case, the frequency spectra was sharply peaked indicating a well-defined periodic signal, whereas in the latter case,

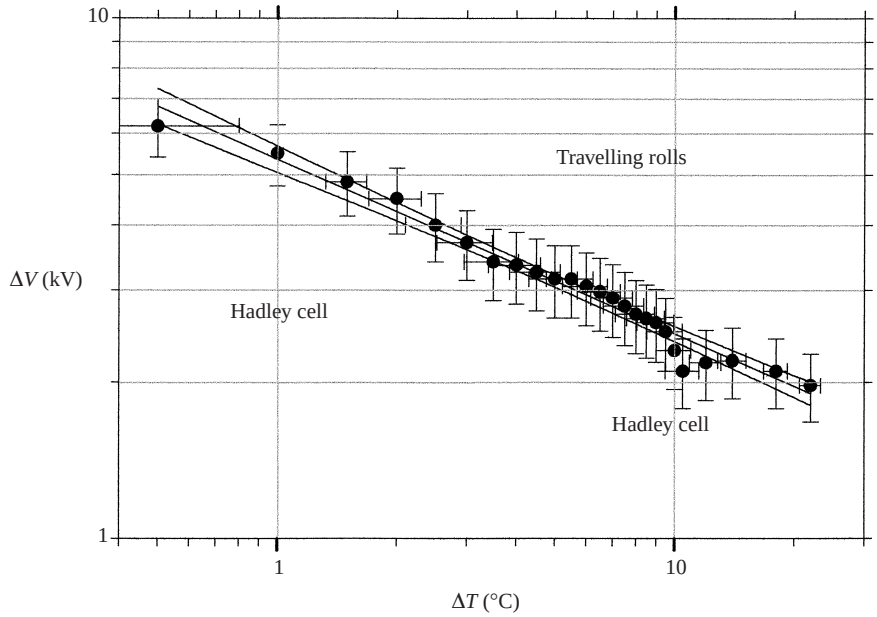

FIGURE 6. Critical voltage amplitudes, ΔV_c, for the onset of travelling rolls as a function of the temperature difference ΔT (data taken at an a.c. frequency of $f = 300\,\mathrm{Hz}$ and an ambient temperature $T_o = 21.6°\mathrm{C}$). The onset values where found by fixing ΔT and increasing ΔV until oscillating roll structures could be seen in the interference pattern. The error bars show the errors of the ΔV and ΔT values. The middle solid line is the fit to the curve: $\Delta V \propto \Delta T^{1/3}$. The lines above and below this line are the limits of the 99% confidence interval. This range is where 99% of the data would fall in repeated measurements based on the statistics of the given data. These limits are used to estimate the error of the exponent, 0.33 ± 0.03. r^2 is the correlation coefficient that is used as a goodness-of-fit parameter, $r^2 = 0.975$.

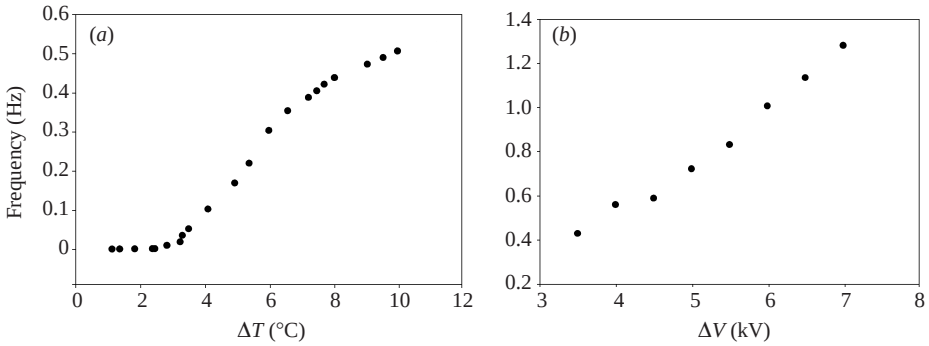

FIGURE 7. Rolls frequency measurements. The oscillating frequencies were measured using a photodiode placed in a given point in the real-time interferogram: (*a*) frequencies measured as a function of ΔT at $\Delta V = 4\,\mathrm{kV}$ with $T_o = 20.0\,°\mathrm{C}$; (*b*) frequencies measured as a function of ΔV with $\Delta T = 22.0\,°\mathrm{C}$ and $T_o = 25.0\,°\mathrm{C}$. These two figures show that the frequency variation is monotonically increasing with ΔT and ΔV.

far above the onset of the travelling rolls, the frequency spectra is broadbanded and the frequencies shown are the peak frequencies. Figure 7(*a*) also shows the behaviour of the frequency as ΔT is increased past the onset of travelling rolls. This shows that the travelling rolls appear as ΔT is increased so that both ΔV and ΔT (or R_g and R_{Emax}) are control parameters for this instability.

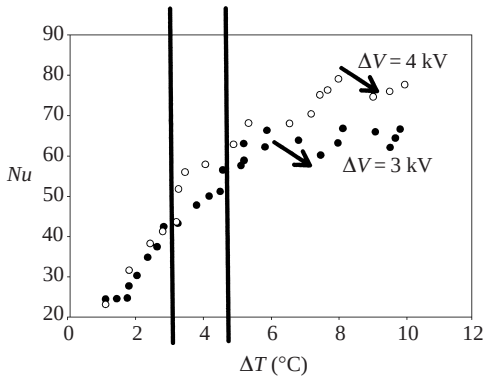

FIGURE 8. Power measurements to the inner sphere allow the Nusselt number, *Nu*, to be measured. Shown above is *Nu vs.* ΔT for two different values of ΔV. The Hadley cell and the propagating rolls both transport heat from the inner sphere. The solid lines show the approximate onset of travelling rolls at 3 kV and 4 kV. The arrows indicate the region where *Nu* decreases at 3 kV and 4 kV.

We have further characterized this flow by measuring the heat transport from the inner sphere. This effect is usually characterized by measuring the Nusselt number (*Nu*), as a function of ΔT. The Nusselt number for heat transfer from the inner sphere is defined as:

$$Nu = \frac{H}{\kappa_s [\partial T/\partial r]_{r_i}} = \frac{H\left(1 - \frac{r_i}{r_o}\right) r_i}{\kappa_s \Delta T}. \tag{5}$$

H is the heat flux transferred between the inner and the outer spheres and κ_s is the heat transfer coefficient for heat conduction, otherwise known as the thermal conductivity. This number is the ratio of the actual heat transfer to the heat transfer that would occur by conduction alone if the fluid remained at rest. Normally, the onset of convection is marked by *Nu* increasing above unity for a bifurcation from a conductive state. The Hadley cell, however, is present at any $\Delta T > 0$ and prevents a conductive state from occurring in our system. Nevertheless, we present *Nu* in figure 8 as a function of ΔT by recording the voltage, V_h, and the current, I_h, to the inner sphere heater. Below $\Delta T = 2\,^{\circ}\mathrm{C}$, the heat transport stays roughly constant, implying that the Hadley flow is steady so that the combined conduction and convection heat transport stays about the same. Above $\Delta T = 2\,^{\circ}\mathrm{C}$, this heat transport increases, probably due to more appreciable Hadley convection. At higher ΔT, corresponding to the onset of travelling rolls, *Nu* increases at a greater rate. This change is more evident at higher ΔV, e.g. at $\Delta V = 3\,\mathrm{kV}$ there is a small change in the *Nu* slope at $\Delta T \cong 5\,^{\circ}\mathrm{C}$, whereas at $\Delta V = 4\,\mathrm{kV}$ the change in the *Nu* slope at $\Delta T \cong 3\,^{\circ}\mathrm{C}$ is larger. More striking is the behaviour of *Nu* far above onset where *Nu* may actually decrease. These decreases appear to be smaller at higher ΔV, e.g. at $\Delta V = 3\,\mathrm{kV}$, *Nu* decreases by $\approx 10\%$ between $\Delta T \approx 6\,^{\circ}\mathrm{C}$ and $\Delta T \approx 7.5\,^{\circ}\mathrm{C}$ whereas $\Delta V = 4\,\mathrm{kV}$ we observed a decrease of $\approx 6\%$ between $\Delta T \approx 8\,^{\circ}\mathrm{C}$ and $\Delta T \approx 9\,^{\circ}\mathrm{C}$. At $\Delta T > 6.61\,^{\circ}\mathrm{C}$ for $\Delta V = 3\,\mathrm{kV}$ and $\Delta T > 5.5\,^{\circ}\mathrm{C}$ for $\Delta V = 4\,\mathrm{kV}$, the roll structures appear disordered is space and time. The appearance of these turbulent rolls correlates with the decrease in *Nu* at $\Delta V = 3\,\mathrm{kV}$ and the levelling of *Nu* at $\Delta V = 4\,\mathrm{kV}$ of figure 8.

We can see that the presence of the Hadley cell complicates the classical method of finding the onset of convection by measuring *Nu* (Ahlers, Berge & Cannell 1993). Because of this, we have also measured a modified Nusselt number Nu^* by calculating,

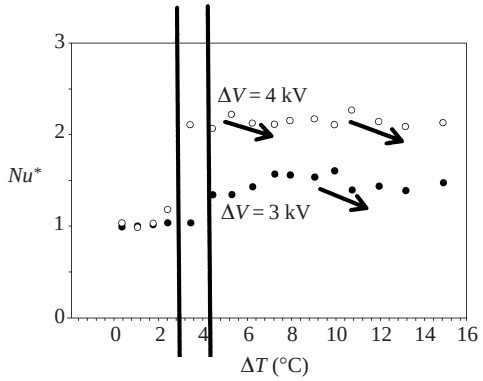

FIGURE 9. Variations of the modified Nusselt number Nu^* *vs.* ΔT for two different values of ΔV and $T_c = 20.0\,^{\circ}\mathrm{C}$. Nu^* more directly indicates the effect of the travelling rolls, since they only exist when ΔV is applied. Below the onset of the propagating rolls, $Nu^* \approx 1$. The large fractional increase in heat transport is due to the travelling roll's convection. The solid lines show the approximate onset of travelling rolls at 3 kV and 4 kV. The arrows indicate the region where Nu decreases at 3 kV and 4 kV.

for each ΔT value, the ratio:

$$Nu^* = \frac{\text{Heat flux with } \Delta V}{\text{Heat flux without } \Delta V} = \frac{H_{\Delta V}}{H_{\Delta V=0}}. \tag{6}$$

In this way, we obtain a dimensionless measure of the heat transport obtained with the presence of the high voltage – and the travelling rolls, if they exist – normalized by the heat transport by conduction and Hadley convection, when $\Delta V = 0$. The results of Nu^* are shown at $\Delta V = 3\,\mathrm{kV}$ and $\Delta V = 4\,\mathrm{kV}$ in figure 9. We can clearly see, in this case, that the onsets of the instability correspond to the values of Nu^* greater than one. The onset values are also approximately the same as shown in figure 6. Below the onset of the propagating rolls, Nu^* is unaffected by ΔV, and above onset, Nu^* increases from the convective heat transport of the propagating rolls. We can also see that the travelling rolls significantly increase the heat transported from the inner sphere (Nu^* increases 30% to 100%) as measured by what it would have been without the travelling rolls. At $\Delta T > 5.5\,^{\circ}\mathrm{C}$ for $\Delta V = 4\,\mathrm{kV}$, where the rolls first appear disordered is space and time, Nu^* begins to decrease. The appearance of disordered rolls at $\Delta V = 3\,\mathrm{kV}$, $\Delta V > 6.61\,^{\circ}\mathrm{C}$, correlates with a slight decrease in Nu^*.

5. Discussion

5.1. *Rayleigh number for dielectric buoyancy*

Because our system has two buoyancy forces we may define another Rayleigh number, R_E, characterizing the buoyancy associated with the electric field gradient. As in R_g, defined above, R_E is the ratio of the buoyancy force to the viscous force. A particular base state that is perturbed in pressure, temperature, velocity, or any combination of these, is unstable if this perturbation grows. Whether a perturbation grows, shrinks or maintains the same amplitude depends on the value of R_E or R_g. The exact value of R_E or R_g where instability occurs could, in principle, be calculated from the equations of motion of the perturbation. The Rayleigh number appears in these equations of motion as a dimensionless control parameter and the value of the critical Rayleigh

number generally depends on the form of the perturbation. We know, however, that an arbitrary perturbation will grow when the buoyancy force can do work on it (put energy into the perturbation) at a rate greater than the viscous force dissipates it (take energy out of the perturbation). In the well-known Rayleigh–Bénard problem, an infinite horizontal layer is subjected to an unstable linear temperature gradient, $\Delta T/d$. A buoyancy force is produced on a fluid particle if it is pushed off its horizontal isotherm by a perturbation. The buoyancy force per unit mass, f_b, of a perturbation is $\beta g \delta T$, where δT is the local temperature change produced by the perturbation. The buoyancy force may be produced by displacing a fluid element a vertical distance of order δz (i.e. $\delta T = (\Delta T/d)\delta z$ or $f_b = \beta g(\Delta T/d)\delta z$). The viscous force per unit mass, f_v, depends on the form of the velocity that results from such a perturbation. Without knowing this velocity, v_z, we can still estimate its value from the convective heat transfer balance (Landau & Lifshitz 1987) to be $v_z \delta T/\delta z \approx D_{th}\delta T/\delta z^2$ or $v_z = D_{th}/\delta z$ so that $f_v \approx \nu v_z/\delta z^2 = \nu D_{th}/\delta z^3$. We obtain, finally, that $f_b/f_v \approx \beta g \Delta T \delta z^4/(\mathrm{d}\nu D_{th}) > 1$ when the instability occurs. The value of δz is also unknown because the order of the size of a perturbation depends on the form of a perturbation. We can see that δz has to be less than d and, in fact, a perturbation that produces a displacement of $\delta z \approx d$ will results in the largest f_b/f_v. This corresponds to the observed cell size in Rayleigh–Bénard convection. Actual perturbations are much smaller than this so that the critical Rayleigh number $R_g^c = \beta g \Delta T d^3/\nu D_{th} \gg f_b/f_v > 1$, and in fact $R_g \sim 1000$ for a horizontal layer, with the exact value depending on the boundary conditions and geometry.

We can use a similar argument to define a control parameter for a perfectly spherically symmetric system with a radial temperature gradient and a central force. In such a system, we would also expect that convection would begin when the dielectric buoyancy force is sufficiently greater than viscosity, or when $f_b/f_v > 1$. In this case where $g = 0$, the base state would be a stationary fluid with heat conducting from the inner to the outer sphere. The temperature distribution is found by solving the Laplace equation with $T(r_i) = T_i$ and $T(r_o) = T_o$,

$$\Delta T'(r) = \frac{\Delta T}{1-\eta}\left(1 - \frac{r_i}{r}\right), \tag{7}$$

where $\eta = r_i/r_o \leqslant 1$, is the radius ratio ($\eta = 0.38$), and $\Delta T'(r) = T_i - T(r)$. We next let a perturbation result in a displacement normal to these steady-state isotherms. Such a radial displacement of a fluid element produces a buoyancy force $f_b = \gamma g_e \delta T = \gamma g_e(r)(\mathrm{d}T'/\mathrm{d}r)\delta r \propto \delta r/r^7$, where δr measures the perturbation size. The radial velocity, from the energy balance in spherical coordinates is $v_r = D_{th}/\delta r$, so that $f_v = D_{th}\nu/\delta r^3$.

As in the horizontal case, we have to make assumptions about the particular perturbation to know δr because there is no natural scale in this problem to measure it. We can, however, consider the largest possible displacement δr of a perturbation. In this case, we consider the largest possible relative outward displacement of $\delta r/r = d/r_i$ of a perturbation and the largest possible relative inward displacement $\delta r/r = d/r_o$ of a perturbation. The characteristic length in the horizontal case, d, refers to the gap where a given ΔT has been externally imposed. In spherical geometry, both the force and the temperature refer to the natural origin present in concentric spheres, so an appropriate length scale is r_i instead of d. In our experiment, r varies between $1 \leqslant r/r_i \leqslant 1/\eta = 2.65$ so that r_i is both an appropriate and convenient length scale. Using this length scale, and because both $\Delta T'$ and g_e depend on position, we obtain

a radially varying Rayleigh number:

$$R_E = \frac{C\Delta V^2 \Delta T}{\left(r/r_i\right)^7}, \quad C = \frac{2\gamma\kappa\varepsilon_0}{\nu D_{th}\,\rho(1-\eta)}\left(\frac{r_o}{d}\right)^2. \tag{8}$$

In this case, as in the horizontal layer case, when R_E is above a threshold value, $R_E \geqslant R_E{}^c$ where perturbations grow, this conductive state is unstable and roll structures grow. Because $g_e \propto \Delta V^2/r^5$ and $\Delta T' \propto \Delta T/r$, R_E depends on ΔV, ΔT and position. R_E reaches a maximum, R_{Emax}, at the surface of the inner sphere where the buoyancy force is largest and where the temperature is highest. It is therefore most likely that unstable perturbations occur at $r/r_i = 1$. In fact, we have only seen the roll structures, like those shown in figures 4 and 5, near the inner sphere. Values of R_{Emax} are given for the images in figure 4 and 5. We can see that in this spherically symmetric case we would expect that at R_{Ec}, $\Delta V_c \propto \Delta T_c^{-1/2}$.

Figure 6 is a set of critical values, $\Delta T = \Delta T_c$ and $\Delta V = \Delta V_c$, for the onset of travelling rolls. In other words, they are a set of points that satisfy the conditions. $R_E(\Delta T_c, \Delta V_c) = R_{Ec}$. Fitting the curve in figure 6 to a power law, however, shows the experimental points, over approximately two decades of ΔT, give the following relation:

$$\Delta V_c \propto \Delta T_c^{-1/3}, \tag{9}$$

where the exponent is -0.33 ± 0.03. If all the other parameters are taken to be independent of position, as in the above case, R_{Ec} is also independent of position, so that at the onset of propagating rolls we should expect that $\Delta V_c \propto \Delta T_c^{-1/2}$. In addition, if R_E depends only on r, ΔT and ΔV, we would expect the rolls to form uniformly around the sphere. The rolls, however, appear in the upper hemisphere, as shown in figure 5, and the rolls consistently start near the equator when either ΔT or ΔV is slowly increased. This implies that R_E must also depend on the polar angle, θ.

5.2. *Polar angle dependence*

The polar angle dependence of the total body force may be inferred from the gradient of the potential in figure 2. Vertically above the central sphere, the polarization force and gravitational force are parallel, adding to a larger net force. Vertically below the central sphere, these same forces oppose each other, producing a smaller net force. Clearly the spherical symmetry of the ideal case is broken even before ΔT or ΔV are applied to the system. The potential in figure 2 shows a saddle point vertically below the sphere (the potential is maximum in the vertical direction and minimum in the horizontal). This is also a point of weightlessness given by the condition $g = g_e = k\Delta V^2/r_w^5$, where the constant k is given in equation (3) and r_w is the weightless radius. This saddle point is a point of stable equilibrium in the vertical direction – with each buoyancy force providing a vertical restoring force – and unstable in the horizontal direction. In this experiment, r_w extends out from the inner sphere only slightly (e.g. $(r_w - r_i/d = 0.04$ at $\Delta V = 4000\,\mathrm{V})$. The cells shown in figures 4 and 5 are approximately an order of magnitude larger. The cell thickness, Δr, may be described by using a dimensionless cell thickness, D, where $D = \Delta r/r_i$. D is estimated from typical images such as those in figures 4 and 5, to be at most $\frac{1}{2}(D < \frac{1}{2})$ for all parameter values used in this experiment. At $D = \frac{1}{2}$ we find that $g_e \approx 0.13\,\mathrm{g}$ at 3000 V and $g_e \approx 0.24g$ at 4000 V. Even though the two forces point mostly in different directions in the flow domain, r_w is a natural scale for separating of the two buoyancy effects, because at $r > r_w$ the gravitational buoyancy is always dominant and at $r < r_w$ dielectric buoyancy is always dominant. In the equatorial

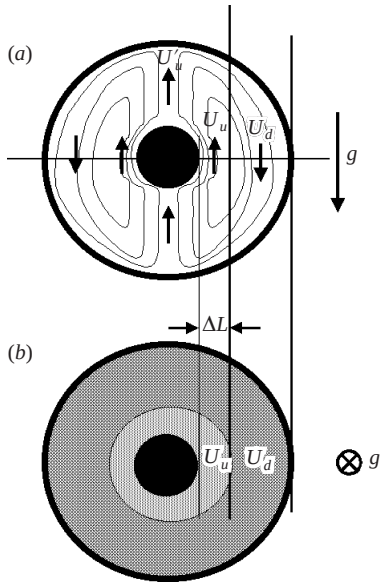

FIGURE 10. A schematic diagram of the Hadley cell flow in a vertical plane with a sketch of the Hadley cell streamlines. This flow breaks the spherical symmetry while retaining azimuthal symmetry. The quantities U_u, U_d and U'_u are also shown. The equatorial planes and definition of the quantity ΔL that is used in the text.

plane, normal buoyancy has no radial component so that the radial buoyancy is totally due to the polarization force. The condition, $g\cos\theta = g_e = k\Delta V^2/r^5$ defines an azimuthally symmetric surface in the bottom hemisphere of zero radial force that includes the saddle point and asymptotically goes to infinity at the equator. Near this surface there is a region where the total radial buoyancy is very small.

The normal buoyancy that causes the background Hadley cell is always present before the onset of travelling rolls, and this flow also breaks the spherical symmetry of the above ideal case, as shown schematically in figure 10. In fact, before the onset of the propagating rolls we can see a polar dependence of the fringe spacing, with the fringes closest together at the bottom pole and the spacing increasing toward the top pole (cf. figure 4). These fringes that roughly correspond to isotherms show that the Hadley convection introduces a polar dependence in the temperature distribution. Below the inner sphere, the azimuthally symmetric Hadley cell makes a cool upward flow toward the bottom pole producing a stagnation point near the bottom pole so that conduction is the dominant heat transfer mechanism at the bottom. The isotherms are compressed at the bottom pole because cool fluid from the Hadley cell arrives at the hot inner sphere. The isotherm spacing increases along the inner sphere as heat is conducted into the fluid from the inner sphere and advected upward by a flow that may have some similarities to a thermal boundary layer. This hot fluid near the inner sphere leaves the inner sphere above the equator, spreading out the isotherms above the inner sphere, as shown in figure 4(*a*).

5.3. *Boundary flow*

Because our system is bounded, analogies with the usual boundary-layer theory are limited, especially because there is no externally imposed velocity and the recirculating fluid is probably driven to a large extent by pressure gradients that violate the

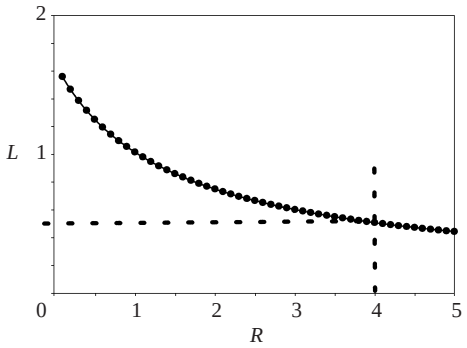

FIGURE 11. The behaviour of $L = \Delta L/r_i$, where ΔL is the distance from the inner sphere to the zero velocity radius in the equatorial plane, as shown in figure 10. The parameter R is the ratio of the average upward velocity, U_u, to the average downward velocity, U_d in this plane. The relation between these two is found by conservation of mass. We can see that L decreases with R in analogy to a boundary layer. Also shown is the R corresponding to $L = 1/2$.

assumption of small pressure gradients in the flow. Nevertheless, the data in figure 5 show that $D(\theta)$ increases along the inner sphere from the bottom pole toward the equator because it traces something that appears similar to a thermal boundary layer around the inner sphere. Because the Prandtl number is $Pr = 10.5$ we would expect such a thermal boundary layer to be relatively thin. However, the fluid is in fact recirculated in the Hadley cell, so this layer may be larger in steady state. In the equatorial plane, there must be both upward-moving hot fluid near the inner sphere and downward-moving fluid near the outer sphere. Taking ΔL to be the radial dimension of the upward-moving region, as shown in figure 10, conservation of mass implies, $U_u[\pi(r_i+\Delta L)^2-\pi r_i^2] = U_d[\pi r_o^2-\pi(r_i+\Delta L)^2]$, where U_u and U_d are the average velocities of the upward- and downward-moving fluid, respectively. To estimate the ΔL, we require the ratio of $R = U_u/U_d$ that is also a measure of the driving of the system by the inner sphere heating. This gives

$$L = \frac{\Delta L}{r_i} = \left[1 + \frac{\eta^2 - 1}{1 + R}\right]^{1/2} - 1, \tag{10}$$

with $\eta = r_o/r_i = \frac{8}{3}$. Figure 11 shows the behaviour of L as a function of the driving as characterized by R. This plot shows that as the driving increases the dimensionless layer width L becomes smaller. This is similar to an open-flow thermal boundary layer that also decreases in width as the external velocity is increased. The downward flow is primarily driven by the reaction pressure gradient from the upward-moving fluid column above the inner sphere. This reaction pressure for an incompressible fluid is an expression of the constraint of mass conservation. The upward-moving column of fluid is driven by normal buoyancy and it has an average upward velocity of U_u' over an area very nearly $\pi(r_i + \Delta L)^2$ for a small inner sphere. The approximate expression for the total upward-moving column of mass, $U_u'\pi(r_i + \Delta L)^2$, is the same as the downward-moving mass, so that $U_u'\pi(r_i + \Delta L)^2 \approx U_d[\pi r_o^2 - \pi(r_i + \Delta L)^2]$. The two upward velocities have different velocity scales. The flow at the equator is similar to a thermal boundary layer, so the velocity scales as $U_u \sim \nu/r_i$. The flow above the inner sphere is similar to thermal convection in a horizontal layer and scales as $U_u' \sim D_{th}/r_i$. We write $U_u' = f(\Delta T)D_{th}/r_i$ and $U_u = g(\Delta T)\nu/r_i$ where the functions f and g are determined by the solution to the equations of motion with an averaging

over the appropriate area. The above conditions give:

$$R = \frac{Pr}{h(\Delta T)} \frac{\eta^2 - 1}{\eta^2}, \quad h(\Delta T) = \frac{g(\Delta T)}{f(\Delta T)}. \tag{11}$$

Figure 11 shows that when L is the cell thickness, $L \approx \frac{1}{2}$ and $R \approx 4$. Using the values, $Pr = 10.5$ and $\eta = \frac{8}{3}$ find that the factor h should be $h \approx 2.3$.

5.4. *Travelling roll onset*

We have also observed that ΔV has an influence on the spacing of the fringes and the shape of the isotherms. Prior to the onset of the propagating rolls, when a smaller ΔV is applied, the fringe spacing decreases, indicating that isotherms become more compressed toward the inner sphere. The dielectric buoyancy clearly influences the Hadley convection before the onset of travelling rolls. If a large ΔV is suddenly applied, this additional buoyancy produces transient rolls that reorganize into travelling rolls. This shows that the steady-state Hadley cell without ΔV may produce a potentially unstable layer even near the bottom pole, where a cell may form. Because the travelling rolls bifurcate from the Hadley cell base flow, the upward motion of the rolls must be caused by both normal buoyancy and the interaction of the new flow from the instability with the Hadley cell. The stress on the Hadley cell from these smaller rolls soon changes the situation so that fluid near the bottom hemisphere of the inner sphere is no longer unstable. Nevertheless, the presence of a roll near the bottom of the inner sphere, where dielectric buoyancy is opposite to the normal buoyancy eliminates normal buoyancy as a possible cause of this instability, although normal buoyancy is clearly influential in its evolution after onset.

Because the travelling rolls are consistently seen to start near the equator and near the inner sphere, this is probably a point in the flow where a perturbed fluid element experiences the most buoyancy and the least viscous resistance (i.e where f_b/f_v is a maximum). As in the previous discussion, we perturb a fluid element to a temperature that differs by δT from the steady temperature distribution before onset. In our experiment, the dielectric buoyancy becomes larger than normal buoyancy near the inner sphere, but never so large as to make normal buoyancy insignificant. The instability, however, occurs close to the inner sphere where the dielectric buoyancy is large and it only occurs when ΔV is applied. We therefore let f_b refer to the dielectric buoyancy for the purposes of discussing the onset. The dielectric buoyancy, f_b, also tends to force fluid elements in the outward radial direction. The viscous force f_v, refers to the force experienced by a perturbation moving relative to the Hadley cell flow. The viscous stress on an outward radial perturbation is azimuthally symmetric in the Hadley cell. It is also smaller in the upper hemisphere (Hadley flow tends to move away from the sphere in the upper hemisphere) than in the lower hemisphere (flow tends to move toward the sphere). At the equator, all of the velocity in the Hadley cell is in the θ-direction so that a perturbed fluid element will be advected by the flow and vertically accelerated by normal buoyancy to a position of different f_b. An adiabatic δT is also changed when the perturbed fluid element is rotated or strained by the base flow. As in the simpler case above, there are several factors in f_b that contribute to its form. As discussed above, the temperature in the fluid, $\Delta T' = T_i - T$ depends on the position (r, θ) and the voltage ΔV, so that we can express the function $\Delta T'$ as $\Delta T' = \Delta T f'(r, \theta, \Delta V)$ where $f'(r, \theta, \Delta V) \approx O(1)$ such that $f' = 0$ at $r = r_i$ and $f' = 1$ at $r = r_o$. The exact form of this function can, in principle, be found from the equations of motion and the energy equation. The function $f_b = \gamma g_e \delta T = \gamma g_e(r)(\mathrm{d}T'/\mathrm{d}r)\delta r$ is also dependent on $(r, \theta, \Delta V)$. The function

f_v also depends on $(r, \theta, \Delta T)$ through the velocity and its derivatives. Therefore, the ratio f_b/f_v depends on $(r, \theta, \Delta V, \Delta T)$. We take the ratio f_b/f_v to be modified from the spherically symmetric case (i.e. with $f_b/f_v = R_E \propto \Delta T \Delta V^2$) by a function $p(r, \theta, \Delta V, \Delta T)$. It then has the form $f_b/f_v = R_E = \Delta T \Delta V^2 p(r, \theta, \Delta V, \Delta T)$. At R_{E^c}, we know from the experiment that p has a maximum at the equator and near the inner sphere where the rolls start. We also know that from equation (7), the relation between ΔV_c and ΔT_c, that $R_E{}^c \propto \Delta V_c \Delta T_c{}^{1/3}$ for onset from the data in figure 6. At onset $R_E{}^c = \Delta T_c \Delta V_c^2 p(r_c, \theta_c, \Delta V_c, \Delta T_c)$ so that $p \propto \Delta T_c^{-2/3} \Delta V_c^{-1}$.

5.5. *Travelling roll frequency and heat transfer*

As reported above, the heat transport increases below the onset of travelling rolls. This increase is caused both by the convective transport from the Hadley cell and the increased local temperature gradient near the inner sphere when ΔV is applied. As ΔT increases, the velocity and velocity gradient near the inner sphere increases so that Nu also increases. Above the onset of travelling rolls, the data shows more scatter. Although the heat flow generally increases as ΔT increases above onset, it sometimes decreases as ΔT increases, as shown in figure 8. Figure 9 shows the ratio of heat transferred with ΔV to the heat transferred without ΔV, (i.e. Nu^*). The ratio measures the influence of the travelling rolls on the heat transfer more directly. The heat transferred from the inner sphere is greatly increased when the travelling rolls first appear, compared to what it would have been without this instability. This is especially true at the higher ΔV. The smaller-scale rolls produce larger average velocity gradients near the inner sphere. This, together with radial flow that pumps hot fluid away from the inner sphere, produces a much larger heat transfer than the Hadley cell. Before the onset of travelling rolls, Nu^* also shows a slight increase. If ΔV had no influence on the heat transported, then Nu^* would be 1 until onset. As discussed above, when ΔV is applied, the fringe spacing decreases, indicating the temperature gradient has also increased. Because the Hadley cell velocity is driven by normal buoyancy, there is more heat convected upward from regions of hotter fluid that are closer to the inner sphere.

Figure 7(a) shows that the frequency of the travelling rolls increases with ΔT as the onset of travelling rolls is crossed. The interferometric and shadowgraphic visualization show, however, that the wavelength of the rolls does not change much with ΔT, showing that the roll velocity increases with ΔT, as it also appears to do on videotape recordings. The fringe contrast also appears to increase near onset, implying that the amplitude of the travelling rolls also increases near onset. The onset of these rolls appears to have some of the usual characteristics of a supercritical Hopf bifurcation. The velocity increase, however, is not typical of such a bifurcation. The velocity increase with ΔT is caused by several affects. First, the Hadley cell velocity should also increase with ΔT so that the stress from the Hadley cell on the travelling rolls increases and the travelling roll velocity increase follows. Secondly, as ΔT increases, the normal buoyancy force that pulls hot fluid upward also tends to increase the travelling roll velocity. These changes in the convection dynamics are also reflected in the significant increase in heat transport shown in figure 8 and 9.

Far above the travelling roll onset ($R_g > 7.9 \times 10^4$ for $\Delta V = 3\,\mathrm{kV}$ and $R_g > 6.6 \times 10^4$ for $\Delta V = 4\,\mathrm{kv}$), the roll structures appear disordered in space and time. We have recorded the time series of these disordered travelling rolls. The Fourier transform of their time series is not a sharp peak, as it is near onset, but is a broadened frequency band that still has a definite peak or maximum. Figure 7(b) shows how this frequency maximum monotonically increases as ΔV is increased. The increase in the

peak frequency of these disordered travelling rolls with ΔV is caused by an average wavelength decrease of the rolls as ΔV is increased. The travelling rolls exist close to the inner sphere in a layer that is defined by a larger $g_e(r)$ where the Hadley cell flow is unstable. The size of this unstable region corresponds to the size of the rolls. When ΔT is kept constant and ΔV increases, the size of this unstable region decreases and so does the typical propagating roll size. The typical roll velocity, however, is defined by the interaction of the Hadley cell and normal buoyancy that stays constant. This constant average velocity with decreasing average wavelength implies an increasing average frequency, as seen in the data. This decrease in roll size corresponds to an increase in roll vorticity, so that more heat may be transported from the inner sphere to the Hadley cell, as can be seen in the two curves of figures 8 and 9 that show more heat transfer at higher voltage.

After the initial increase in heat transfer at the onset of travelling rolls, the heat transport coefficient both increases and decreases with increasing ΔT. This happens both in terms of Nu and Nu^*, shown in figures 8 and 9. A comparison of these two figures shows that these decreases do not always occur in the same temperature intervals. At 3 kV, for example, Nu decreases in the interval $6 < \Delta T < 7.5$ while Nu^* slightly increases in the same interval. In this interval, the travelling rolls continue to increase the relative heat transfer, while the absolute heat transfer from both flows is decreasing. This suggests that the heat convected by the travelling rolls is not being transported to the Hadley cell. The travelling rolls and the Hadley cell are not mixing fluid as vigorously as at lower ΔT so that more heat remains in the travelling roll region. The flow may have made another bifurcation that results in the decrease in heat transport. A bifurcation that breaks the azimuthal symmetry, for example, should decrease the kinetic energy of the radial component of velocity flow to create azimuthal flow so that less heat is transported to the Hadley cell and more heat remains in the travelling roll region. As discussed in Hegseth (1996), the Reynolds stress from a spatially separated turbulent region may strongly influence the laminar flow. We expect such spatially separated turbulent and laminar flows (Hegseth 1996) in this system at higher R_E and R_g. The Reynolds stress from the turbulent roll structures may be forcing the mean flow of the Hadley cell around the turbulence so that more heat remains in the turbulence and less heat is transported from the inner sphere.

6. Conclusion

The fluid in this system has two forces applied to it when it is heated, one large scale and one small scale. A large-scale axial force from normal buoyancy always drives a Hadley cell in the fluid. A smaller-scale radial force from dielectric buoyancy drives the travelling rolls at all ΔT when sufficiently large ΔV is applied. The conditions for the onset of the smaller-scale travelling roll instability must come from the larger-scale Hadley cell and the detailed structure of this flow is probably the cause of the power law relation $\Delta V \sim \Delta T^{-1/3}$. The Hadley cell drives the travelling rolls so they travel upward, while this small-scale flow pumps hot fluid into the Hadley cell, producing a large increase in heat transfer.

There are some similarities between this system and large-scale geophysical flows. This system has some similarities to a planetary liquid outer core subjected to a strong external gravitational field. The radial force in spherical geometry together with a mixing convective layer near the inner sphere also has some similarities to the atmospheric boundary layer (Sorbjan 1989). Although this system has significantly

different geometry from most atmospheres, a planet may have a thin unstable layer near the planetary surface surrounded by a thicker stable layer, as in the case of the earth. Our system also has an unstable layer close to the surface, surrounded by a stable flow in the outer layer. In fact, the earth also has a large-scale Hadley cell, driven by the large-scale horizontal temperature gradient from the non-uniform heating of the sun. The large heat transport increase from the inner sphere shown in our experiment shows that this surface convection can be quite important in such a system, i.e. a highly conductive solid in contact with less conductive fluid still loses significant heat when convection is present. Another interesting result is the decrease in heat transport at larger ΔT.

We gratefully acknowledge the support of NASA through NASA-OBPS grants NAG3-1915 and NAG3-2447.

REFERENCES

Ahlers, G., Berge, L. I. & Cannell, D. 1993 Thermal convection in the presence of a first-order phase change. *Phys. Rev. Lett.* **70**, 2399–2402.

Carrigan, C. R. & Busse, F. H. 1983 An experimental and theoretical investigation of the onset of convection in rotating spherical shells. *J. Fluid Mech.* **126**, 287–311.

Chandrashakar, S. 1961 *Hydrodynamic and Hydromagnetic Stability*. Oxford University Press.

Cloot, A. & Lebon, G. 1990 Marangoni convection in a rotating spherical geometry. *Phys. Fluids* A **2**, 525–531.

Cushman-Roisin, B. 1994 *Introduction to Geophysical Fluid Dynamics*. Prentice-Hall.

Fletcher, C. A. J. 1991 *Computational Techniques for Fluid Dynamics*. Springer.

Guyot, G. 1998 *Physics of the Environment and Climate*. Wiley.

Hart, J. E. 1976 Studies of earth simulation experiments. *NASA-Contractor Rep.* CR-2753.

Hart, J. E., Glatzmaier, G. A. & Toomre, J. 1986 Space-laboratory and numerical simulations of thermal convection in a rotating hemispherical shell with radial gravity. *J. Fluid Mech.* **173**, 519–543.

Hegseth, J. 1996 Turbulent spots in plane Couette flow. *Phys. Rev.* E **54**, 4915–4926.

Hegseth, J., Garcia, L. & Amara, M. K. 1999 A compressible geophysical flow experiment. *Fourth Microgravity Fluid Physics Conference*, NASA Conf. Proc. also avilable at the following web page: http://www.ncmr.org.

Hegseth, J., Rashidnia, N. & Chai, A. 1996 Natural convection in droplet evaporation. *Phys. Rev.* E **53**, 1640–1643.

Landau, L. D. & Lifshitz, E. M. 1960 *Electrodynamics of Continuous Media*. Addison-Wesley.

Landau, L. D. & Lifshitz, E. M. 1982 *Statistical Physics Part 1*. Pergamon.

Landau, L. D. & Lifshitz, E. M. 1987 *Fluid Mechanics*. Pergamon.

Lorenz, E. N. 1976 Deterministic non-periodic flow. *J. Atmos. Sci.* **20**, 1976.

Minier, J. P. 1998 Large eddy simulation of compressible turbulent flow. In *Advances in Turbulence Modelling*, Von Kármán Lecture Series (ed. D. Olivari), pp. 137–154. Von Kármán Institute.

Pedlosky, J. 1979 *Geophysical Fluid Dynamics*. Springer.

Sorbjan, Z. 1989 *Structure of the Atmospheric Boundary Layer*. Prentice Hall.

Stratton, J. A. 1941 *Electromagnetic Theory*. McGraw-Hill.

Vest, C. M. 1979 *Holographic Interferometry*. Wiley.